



Projected wave climate of Bass Strait and south-east Australia by the end of the twenty-first century

Jin Liu¹ · Alberto Meucci¹ · Ian R. Young¹

Received: 4 December 2021 / Accepted: 21 April 2022 / Published online: 24 May 2022
© The Author(s) 2022

Abstract

A high-resolution third-generation wave model based on unstructured grids, WAVEWATCH III (WW3), was used to study the projected future wave climate of Bass Strait and south-east Australia under two different greenhouse gas emission scenarios (SSP1-2.6 and SSP5-8.5). The wave model, forced with winds from the Australian ACCESS-CM2 Global Climate Model, shows good agreement with coastal long-term buoy observations and an independent WW3 hindcast dataset over the historical period 1985–2014. The projected mean significant wave height (H_s) for SSP5-8.5 by the end of the twenty-first century (2071–2100) shows a robust increase for the majority of the domain, but a decrease in nearshore regions, mainly due to projected decreases in local wind speed. The increase in H_s for SSP1-2.6 is relatively small. Seasonal variations show that H_s (SSP5-8.5) is primarily influenced by Southern Ocean swell in spring and winter and local winds prevail in summer and autumn. H_s percentiles show a stronger increase in extreme wave climate for SSP5-8.5 than for SSP1-2.6. Extreme value H_s for SSP1-2.6 shows a projected decrease in western regions of the domain and an increase in the east. Extreme value H_s for SSP5-8.5 shows a decrease in the nearshore areas of Victoria. This study shows that projected wave climate changes in south-east Australia may have potential implications for Tasmanian and Victorian coastline stability.

Keywords Wave climate · Wave projection · SSP1-2.6 · SSP5-8.5 · WAVEWATCH III · South-east Australia

1 Introduction

Exploring projections of future wave climate is important for many reasons. Changes in future wave climate have potentially major impacts on beach morphology, nearshore sediment transport, and coastline erosion (Hemer et al. 2013c; Morim et al. 2018, 2019; O’Grady et al. 2021). Studying future projection of wave climate is essential for coastal adaptation strategies in densely populated regions (Kirezci et al. 2020), as projected sea-level and coastal flooding are also influenced by wave climate changes (Kirezci et al. 2020; O’Grady et al. 2021). A number of studies have also highlighted the importance of potential changes in the future wave climate on offshore industries (Hemer et al. 2013b; Akpınar et al. 2016; Liu et al. 2022). In addition, potential changes in wave climate may alter relationships with

large-scale climate indices, which have broad implications for both offshore and nearshore dynamics (Hemer et al. 2013c).

Over the last decade, a number of studies have investigated the future wave climate at both regional (Casas-Prat and Sierra 2013; Hemer et al. 2013a; Shimura et al. 2015; De Leo et al. 2021) and global scales (Hemer et al. 2013b, 2013c; Morim et al. 2018, 2019; O’Grady et al. 2021) by using spectral wave models forced with General Circulation Model projected winds. Multi-model ensemble studies showed that the projected mean significant wave height (H_s) will increase in the Southern Ocean (Hemer et al. 2013b, 2013c; Morim et al. 2018). Statistically robust changes in wave climate have also been measured over the last 30 years in the Southern Ocean (Young and Ribal 2019; Young et al. 2020) and extreme wave heights are projected to increase due to the intensification and poleward movement of the westerlies (Meucci et al. 2020; Lobeto et al. 2021; O’Grady et al. 2021).

The south-east Australia wave climate is significantly influenced by the Southern Ocean and the Victorian coast (Fig. 1a) is one of the most densely populated regions in Australia

✉ Ian R. Young
ian.young@unimelb.edu.au

¹ Department of Infrastructure Engineering, University of Melbourne, Melbourne, VIC, Australia

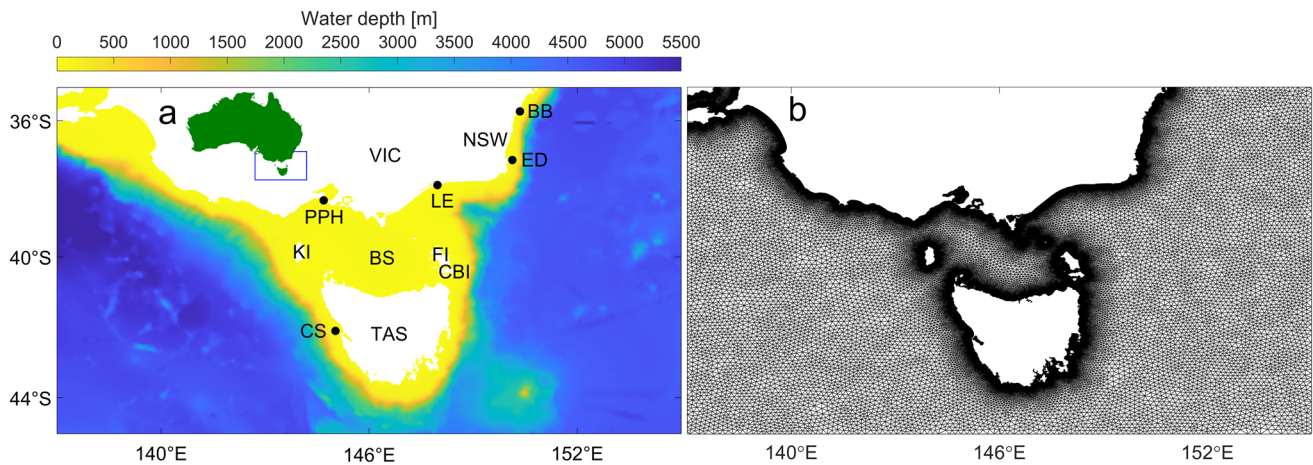


Fig. 1 Water depth (a) and unstructured grids (b) of the research domain (Liu et al. 2022). The insert is the Australian continent with a blue line that marks the open boundary conditions provided by the global wave model (Meucci et al. 2022). NSW New South Wales,

VIC Victoria, TAS Tasmania, KI King Island, FI Flinders Island, CBI Cape Barren Island, BS Bass Strait. Black points mark the buoy locations for model validations. BB Batemans Bay, ED Eden, LE Lakes Entrance, PPH Port Phillip Heads, CS Cape Sorell

(Morim et al. 2016). Understanding the projected future wave climate in this region is crucial to the local community. However, no regional high-resolution studies have been undertaken to assess the potential future wave changes in this region.

In the present study, a high-resolution third-generation wave model was employed to study projections of the future wave climate in this region under two greenhouse gas emission scenarios. In each case, the wave model was forced with winds from the ACCESS-CM2 global climate model (GCM) (Bi et al. 2020). The research domain (137–155° E, 35–45° S) covers Victoria, Tasmania, and southern New South Wales (Fig. 1a). The surrounding islands consist of King Island, Flinders Island and Cape Barren Island in Bass Strait.

This paper is arranged as follows. Section 2 describes the wave model and datasets used. Section 3 shows the model validation for the historical period. Projections of future mean conditions, seasonality and extreme wave conditions are discussed in Sect. 4, followed by conclusions in Sect. 5.

2 Data and methods

2.1 Ocean wave model

The third-generation wave model, WAVEWATCH III (WW3) (WW3DG 2019), was used in the present study. It solves the action density balance equation (WW3DG 2019),

$$\frac{dN}{dt} = \frac{S_{\text{tot}}}{\omega}, \quad (1)$$

where t is time, N is the wave action spectrum, ω is frequency, S_{tot} is the total source term which can be described as,

$$S_{\text{tot}} = S_{\text{ln}} + S_{\text{in}} + S_{\text{wc}} + S_{\text{sw}} + S_{\text{nl}} + S_{\text{bot}} + S_{\text{db}}, \quad (2)$$

where S_{ln} is linear input, S_{in} is wind input, S_{wc} is white-cap dissipation, S_{sw} is swell dissipation, S_{nl} is nonlinear wave-wave interactions, S_{bot} is bottom friction, S_{db} is depth-induced wave breaking.

In the present study, the WW3 model was initiated from quiescent conditions with the linear input source term (S_{ln}) following Cavaleri and Rizzoli (1981). Bottom friction (S_{bot}) was implemented following Hasselmann et al. (1973), with the default JONSWAP bottom friction coefficient. The parameterization of depth-induced wave breaking (S_{db}) was modeled based on Battjes and Janssen (1978). Additionally, the ST6 source term package was used to define the wind input, white-cap, and swell dissipation (Rogers et al. 2012; Zieger et al. 2015; Liu et al. 2019). The ST6 package has few “tunable” parameters. The wind input term does, however, include a factor, $CDFAC$ that modifies the drag coefficient, C_d which relates the wind speed, U_{10} at an elevation of 10 m to the friction velocity, u_* . Meucci et al. (2022) tested values of $CDFAC$ and determined that for ACCESS-CM2 GCM winds, as adopted here, $CDFAC = 1.0$ produced acceptable results in the Southern Ocean. Hence, this value was adopted in this study.

In general, nearshore wave modelling requires high spatial resolution, which can be achieved either by using a high-resolution unstructured grid or a system of nesting models. In this study, an unstructured grid was adopted to resolve the complex bathymetry in the domain. The approach proposed by Roberts et al. (2019) was used to construct the unstructured grid (Fig. 1b), which determining the mesh based on topographic length scale, distance/feature size, wavelength, and channel thalwegs/polylines. The unstructured grid

includes 97,276 nodes and 184,195 elements. As a result, the model grid has relatively high resolution in coastal regions (approximately 400–900 m), whilst retaining coarse resolution in the open ocean, thus greatly improving the computational efficiency of the WW3 model. This unstructured grid was successfully employed by Liu et al. (2022) to model hindcast wave datasets in the same domain.

The WW3 model spectrum was discretized into 36 direction bins with a direction step of 10° and 35 frequency bins, logarithmically distributed from 0.037 to 0.953 Hz. The present model was nested within a global wave climate model, which provided wave spectral data at 85 open boundary locations (Meucci et al. 2022). This global WW3 model used a spatial resolution of 0.5° and the same physics package as the regional wave climate model. The wind field over the computational domain was defined by the ACCESS-CM2 CMIP6 GCM (Bi et al. 2020). Both boundary conditions and wind fields were input at 3-hourly intervals. High-resolution bathymetric data that combined nearshore data from the Victorian Coastal Digital Elevation Model (VCDEM 2017) and is distributed by the Australian Ocean Data Network (AODN, <https://portal.aodn.org.au/>) and offshore data from the Australian Bureau of Meteorology (BOM, <http://www.bom.gov.au/>) were used to define the unstructured bathymetric grid.

After spinning up the WW3 model for a period of 1 month, it was run over three 30-year time-slices with a time step of 20 min. These time slices consisted of (a) the historical period 1985–2014 and the future period 2071–2100 with two different emission scenarios, (b) the mitigation measure scenario (Paris Agreement) SSP1-2.6, hereafter SSP126, and (c) the high emission scenario SSP5-8.5, hereafter SSP585. The following wave parameters were output by the model: significant wave height H_s , peak wave direction D_p (the direction at which the wave energy spectrum reaches its maximum), peak wave frequency, and partitioned wave height parameters (wind wave and primary swell). The reciprocal of the peak wave frequency is the peak wave period T_p .

2.2 Wind fields

There are a range of CMIP6 GCMs which could be used to provide projected winds for the two climate scenarios. Meucci et al. (2022) evaluated the performance of 42 GCMs' surface wind speed data against ERA5 reanalysis winds (Hersbach et al. 2020), using Watterson (2015) M skill score analysis. Meucci et al. (2022) calculated the average M-score of four variables: the sea level pressure, the two wind components, and the modulus of the wind speed. Based on the average of these four M-scores, the ACCESS-CM2 GCM ranked 15th among the 42 models. As such, we conclude that the ACCESS-CM2 wind climate performs

reasonably well globally and is expected to have even better performance in the local Australian region, as it is an Australian-community GCM. Thus, the present model is nested within the Meucci et al. (2022) GCM, and forced by the 3-hourly surface winds from ACCESS-CM2.

It is important to note that, the GCM's sea-ice concentration may also play a role in the present study, as the Southern Ocean wave climate impacts the present model boundary conditions. Meucci et al. (2022) tested the impact of different sea-ice concentrations on the Southern Hemisphere wave climate. They found a 10% change in peak wave period between the ACCESS-CM2 and the EC-Earth3 sea-ice concentration test runs in the region of interest for the present regional model. The differences are particularly evident in the period of the Antarctic sea-ice maximum extent (September).

To evaluate the performance of the present regional climate model, we use ERA5, a state-of-art reanalysis developed by ECMWF (Hersbach et al. 2020). The ERA5 monthly averaged wind speeds were used to evaluate the climate model performance over the historical period (1985–2014). As the present study employed a high-resolution unstructured grid, it is possible to find unstructured nodes close to every ERA5 grid point within the computational domain.

Wave climate models generally have bias compared to reanalysis data associated with wind forcing and bias correction approaches are sometimes applied to address these issues. Hemer et al. (2012) reported that mean conditions and seasonality of wave climate can be improved by adjusting wind speed and direction, while the bias-adjusted winds do not improve extreme wave modelling. Hemer et al. (2013c) further reported that future wave projections under high emission scenarios are relatively insensitive to wind adjustment, and extreme wave simulation can deteriorate with wind adjustment. Therefore, as we primarily concentrate on changes in wave climate (future projection minus present day) rather than absolute values, and as the bias-correction approaches are somewhat arbitrary, no wind correction method was used in this study.

2.3 Buoy observations and WW3 hindcast model data

Long-term buoy data within the domain were used to validate the WW3 climate model. The data were obtained from the AODN website, Gippsland Ports (GP, <https://www.gippslandports.vic.gov.au/>) and the Port of Melbourne (POM, <https://www.portofmelbourne.com/>). The locations of the buoys are shown in Fig. 1a. Detailed information for the buoy data is shown in Table 1.

In addition, Liu et al. (2022) generated an hourly WW3 hindcast dataset (covers 1981–2020) in the same domain with the same model configuration. The hindcast model data

were extensively validated against a buoy network along the Victorian coast (Liu et al. 2022). These hindcast data were also used to validate the present WW3 climate model results.

2.4 Extreme wave analysis

There are many approaches which can be used to determine extreme value estimates of wave conditions. The aim of such approaches is to fit a probability distribution function (PDF) to measured or modelled extreme values and extrapolate to the desired probability level (Coles et al. 2001). With a 30-year wave dataset, it is possible to employ either a peaks-over-threshold (POT) or annual maxima approach to estimate extreme wave conditions for different return periods (Coles et al. 2001; Takbash et al. 2019; Young et al. 2020). The POT approach maximizes the available data and does not exclude multiple peaks in a given year (Takbash et al. 2019). Takbash et al. (2019) estimated extreme wave height with different methods and found that POT-based approaches yield results consistent with long-term buoy observations. Based on this precedence, the POT approach has been used in this study, although it should be noted that all extreme value approaches have associated statistical uncertainty and the estimates have associated confidence intervals.

For the POT approach, a generalized Pareto distribution (GPD) is fitted to the model data with a user-defined threshold value,

$$F(x) = 1 - \left[1 + k \left(\frac{H_s - A}{B} \right)^{-1/k} \right], \quad (3)$$

$F(x)$ is the PDF, k and B are the shape and scale parameters, respectively. A is the user-defined threshold value, which should be high enough to not excessively bias the PDF but not so high as to result in too few data points to form a stable fit of Eq. (3). The choice of the threshold value can impact extreme value estimates (Beguería 2005). Values representing the 90th or 95th percentile values are commonly selected as the threshold value (Takbash and Young 2019; Takbash et al. 2019; Young et al. 2020). Liu et al. (2022) also tested

represents an optimal choice for POT analysis based on hindcast model results in the study domain. Following Liu et al. (2022), the 95th-percentile H_s was selected as the threshold value for the domain. Furthermore, the time between peaks should be typically longer than 48 h to ensure data independence (Caires and Sterl 2005). The probability of exceedance (P) can be represented as (Takbash et al. 2019),

$$P(x < x^{N_{RP}}) = 1 - \frac{N_Y}{N_{RP} \cdot N_{POT}}, \quad (4)$$

where N_{POT} is the number of points involved in the POT approach, N_Y ($=30$) is the total number of years. Here, the return period, N_{RP} , was taken as 10, 20, 50, and 100 for 10-year, 20-year, 50-year, and 100-year return periods, respectively.

3 Model validation

Before investigating future wave projection in south-east Australia, it is essential to validate the modelled wave parameters for the historical period. The ERA5 reanalysis datasets over the historical period (1985–2014) were used to verify the historical climate model (GCM) winds. When comparing reanalysis and climate winds (or waves) it is not possible to consider values at a specific location on a specific date. Climate model winds, unlike hindcast or reanalysis models, are not constrained by measured values of sea-surface temperature and other parameters, and hence have different phase. That is, the values of wind speed on a given day can be quite different. The climate model should, however, be able to reproduce wind and wave climate at a given location. To obtain a representation of the performance of climate model winds over the computational domain, mean monthly values over the historical period (1985–2014) at each ERA5 grid point were determined for both ERA5 reanalysis winds and ACCESS-CM2 climate winds. Figure 2 shows a joint probability (density plot) of wind speeds between ACCESS-CM2 and ERA5. The results show that

Table 1 Detailed information of buoy data. Only data from 1985 to 2014 were considered. *AODN* Australian Ocean Data Network, *GP* Gippsland Ports, *POM* Port of Melbourne, H_s significant wave height, T_p peak wave period, D_p peak wave direction

Location	Longitude (°E)	Latitude (°S)	Duration	Depth (m)	Source	Parameters
Batemans Bay	150.35	35.72	27/05/1986–31/12/2015	71.51	AODN	H_s, T_p, D_p
Eden	150.13	37.17	08/02/1978–31/12/2017	80.23	AODN	H_s, T_p, D_p
Lakes Entrance	147.97	37.91	23/08/2007–31/10/2020	20.37	GP	H_s, T_p, D_p
Port Phillip Heads	144.69	38.36	14/12/1993–11/11/2020	27.72	POM	H_s, T_p
Cape Sorell	145.03	42.12	07/01/1998–31/12/2017	98.44	AODN	H_s, T_p

different threshold values and found the 95th percentile H_s

wind speeds of ACCESS-CM2 are higher than ERA5 for

high mean monthly wind speeds. Further analysis indicated that this generally corresponded to wind forcing in the southern part of the domain. On the contrary, the climate model wind speeds for low values of mean monthly wind speed are underestimated compared to ERA5. Although forming mean monthly values, as undertaken here, reduces variability due to phase differences between reanalysis and climate models, variability will still be potentially large. The results in Fig. 2 do, however, provide an indication of the general performance of a typical climate model GCM in reproducing mean monthly wind speed statistics.

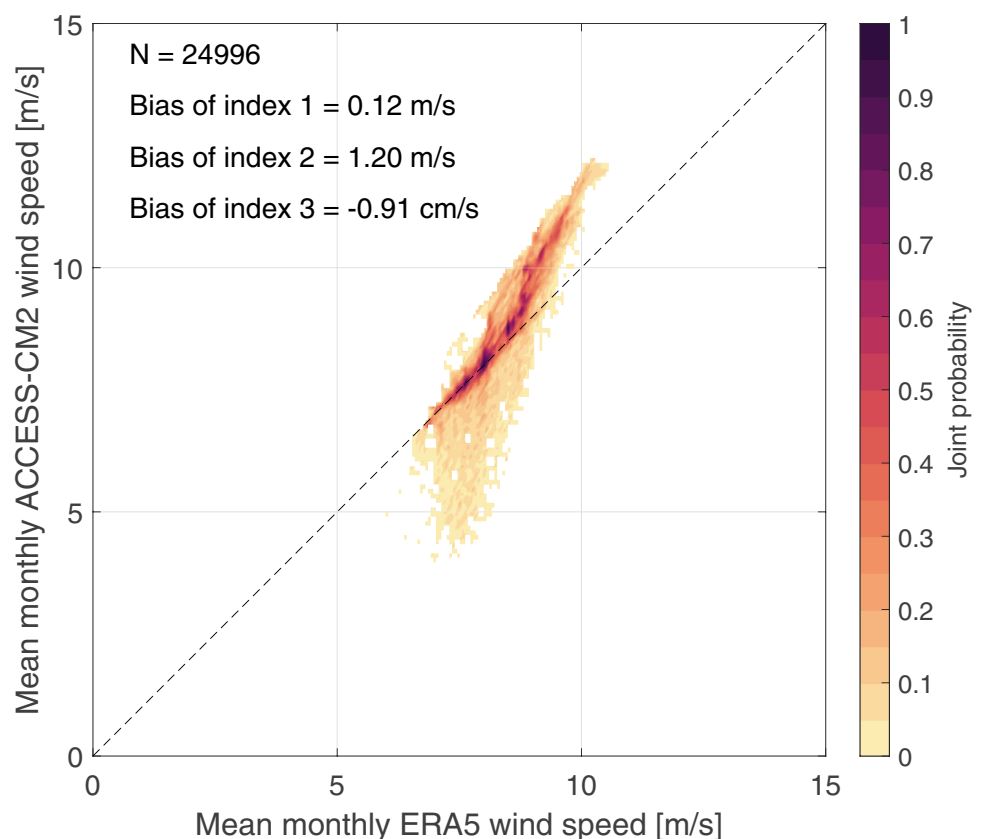
The WW3 hindcast model (Liu et al. 2022), used the same settings as the present model but was driven by ERA5 reanalysis winds with the open boundary conditions taken from a global hindcast model (Liu et al. 2021). This hindcast model was extensively validated against coastal buoy observations over the period 1981–2020. The good agreement found by Liu et al. (2022) indicates that the current model settings are adequate to capture wave characteristics in the domain.

In the present study, the WW3 climate model was validated over the historical period (1985–2014) within the domain. Here, all available long-term buoy observations and WW3 hindcast data at the buoy locations are used to validate the model over the period 1985–2014 (Fig. 3). Three wave parameters were considered in the present study, H_s , T_p and

D_p . For each parameter, mean monthly values, averaged over the full 30-year historical period are compared. The detailed model skill metrics of Batemans Bay and Eden are shown in Table 2.

The climatological comparisons of H_s (Fig. 3a–e) show good agreement of the wave climate model with buoy observations and hindcast model data at the buoy locations. Cape Sorell, which is exposed to the Southern Ocean, shows larger values of H_s (Fig. 3e) for the climate model. This is consistent with global results from Meucci et al. (2022), which indicates that the ACCESS-CM2 forced global model, which defines the boundary conditions for the present regional model, over-estimates the wave climate in the Southern Ocean compared to altimeter and reanalysis results. The other four locations, protected by Tasmania, show slightly smaller values of H_s for the climate model (Fig. 3a–d). Note that, the lower values of H_s for the climate model at the Lakes Entrance and Port Phillip Heads sites may partly be attributed to their relatively shallow water depths (Table 1). However, the smaller values of H_s generated by the climate model for Batemans Bay to Port Phillip Heads, are likely caused by underestimated wind forcing in the northeast of the domain (Liu et al. 2022). This may also be an indication that the resolution of the GCM is limited in its ability to accurately reproduce wind fields nearshore. Compared to the hindcast model (Liu et al. 2022), H_s from

Fig. 2 Density plot of mean monthly values of wind speed between the ACCESS-CM2 climate model and the ERA5 reanalysis over the historical period (1985–2014). Index 1 = climatological mean of annual values, index 2 = mean seasonal amplitude, index 3 = linear trend of annual values (Hemer and Trenham 2016)



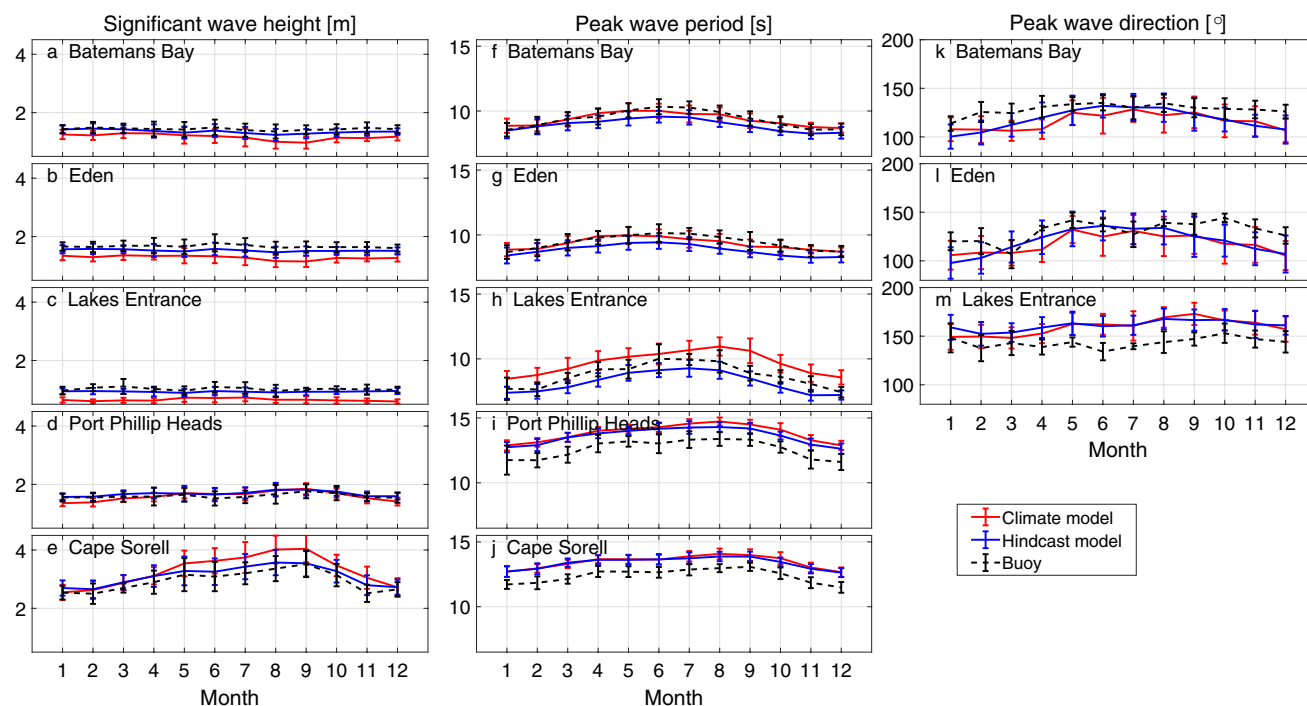


Fig. 3 Climatological comparisons of **a–e** significant wave height, **f–j** peak wave period and **k–m** peak wave direction (degrees clockwise from true north) between buoy observations, hindcast wave model and climate wave model. The values shown are monthly averages

Table 2 The performance of hindcast and climate models against buoy observations. *BB* Batemans Bay, *ED* Eden. Index 1=climatological mean of annual values, index 2=mean seasonal amplitude, index 3=linear trend of annual values (Hemer and Trenham 2016).

		Bias of index 1		Bias of index 2		Bias of index 3	
		Hindcast—buoy	Climate—buoy	Hindcast—buoy	Climate—buoy	Hindcast—buoy	Climate—buoy
H_s [m, m, cm/y]	BB	− 0.08	− 0.27	− 0.07	0.05	0.44	0.43
	ED	− 0.14	− 0.39	− 0.09	− 0.03	0.29	0.28
T_p [s, s, s/y]	BB	− 0.44	− 0.02	− 0.50	− 0.46	0.00	0.00
	ED	− 0.58	− 0.11	− 0.44	− 0.42	− 0.01	0.00

the WW3 climate model are ~10% higher in the southwest portion of the domain and ~10 to 25% lower in Bass Strait and nearshore regions of eastern Victoria (not shown). This is consistent with the point comparisons at the buoy locations in Fig. 3a–e.

The wave climate model historical values of T_p (Fig. 3f–j) follow a similar pattern to H_s (Fig. 3a–e). Although the T_p values from the climate model are slightly lower than the buoy data at Batemans Bay and Eden in winter (June, July, August), they are actually in better agreement than the WW3 hindcast model (Table 2). From Lakes Entrance to Cape Sorell, the values of T_p from the climate model are higher than the buoy observations. Similar to H_s , this appears to be associated with an overestimate in the magnitude of

over the historical period 1985–2014. The vertical error bars represent \pm one standard deviation. The units are shown at the top of each set of panels. The locations are shown on each panel

Units of indexes 1–3 are shown on the first column. There is not enough buoy data at other locations to calculate indexes 1–3. The D_p buoy data at BB and ED are too short to calculate indexes 1–3

Southern Ocean swell in the climate model. The discrete frequency resolution of the buoy observations also limits the T_p comparisons to an accuracy of ~2 s (Young 1994; Liu et al. 2022), which partly explains the phase differences between the climate model and buoys in Fig. 3f–j.

Figure 3k–m shows the comparisons of D_p from Batemans Bay to Lakes Entrance (note there are no directional buoy measurements for Port Phillip Heads and Cape Sorell). The results show that, for the climate model, D_p for Batemans Bay and Eden is more counter-clockwise than the buoy measurements, while the direction at Lakes Entrance is more clockwise. This is consistent with the wave hindcast results (Liu et al. 2022) and validations of the ACCESS-CM2 GCM (Meucci et al. 2022). The directional differences between

the climate model and buoy observations are up to $\sim 20^\circ$ (Fig. 3k–m). Although the directional resolution of buoys should be less than 20° (Young 1994), combined with the 10° directional resolution of the model, means that such directional differences are not unexpected. The D_p bias at Lakes Entrance could also be partly related to its shallow water depth and reduced time coverage of the validation period (2007–2014) at this location.

As noted above, a climate model cannot be used to “hindcast” results on a given day. Rather, they can be used to model climatological values but will generally be less accurate than a hindcast model due to model resolution and the measured data which constrains hindcast and reanalysis models. Noting these limitations of GCMs, the WW3 climate model does capture the wave characteristics over the historical period (1985–2014). The simulated wave parameters show reasonable agreement with the WW3 hindcast data and buoy observations. As such, the validation results add confidence in using the regional wave model, forced with the ACCESS-CM2 GCM, to project the future wave climate in the domain.

4 Future wave climate

After validating the model forced by the ACCESS-CM2 winds for the historical period, the regional wave climate is projected to the end of the twenty-first century (2071–2100) under two greenhouse gas scenarios (low-emission scenario SSP126 and high-emission scenario SSP585). The mean conditions, seasonality, and extreme wave conditions (upper percentiles and return period values) for the period 2071–2100 are then compared with the historical period (1985–2014).

4.1 Mean conditions

The mean values of H_s , T_p and D_p over the historical period (1985–2014) within the domain are shown in Fig. 4a–c. The results show that the southwest part of the domain is dominated by long-period Southern Ocean swell from the southwest. Bass Strait and the north-eastern part of the domain are protected by Tasmania, however, and show lower values of H_s and T_p . Also, D_p changes significantly within Bass Strait and east of Tasmania, as a result of the protection provided by the island. These characteristics of the three wave parameters are consistent with the WW3 hindcast results in Liu et al. (2022).

The projected changes in mean H_s for SSP126 by the end of the twenty-first century show small increases between 1 and 3% across most of the domain (Fig. 4d). For SSP585, there are increases in H_s in the offshore regions of the southern and eastern portions of the domain. Along the coasts of

eastern Victoria and New South Wales and western parts of the domain, however, there is a projected decrease in mean H_s (Fig. 4g). The decrease in mean H_s for SSP585 is the result of a projected decrease in local winds (see Supplementary material Figs. S1e, S2c). Projections of partitioned wave quantities show that for SSP126, wind waves (Fig. S1c) have a greater impact on H_s than swell (Fig. S1d), whilst for SSP585 both wind wave and swell changes are important for H_s .

Values of T_p for both SSP126 and SSP585 scenarios show increases across most of the domain except Bass Strait and the nearshore regions near Lakes Entrance that are protected by Tasmania. These increases in T_p are significantly larger for SSP585 than SSP126 (4% compared to 1%) and are a result of the projected increases in the wave climate and associated swell in the Southern Ocean (Morim et al. 2018; Meucci et al. 2022).

The projected changes in mean D_p for SSP126 (Fig. 4f) show a small counter-clockwise rotation of the waves in the western regions and a stronger clockwise rotation in the protected (swell shadow) regions (east of Tasmania). For the nearshore regions of north-eastern Tasmania, there is also projected to be a counter-clockwise rotation. It is worth noting that the spatial distributions of projected changes in mean D_p for SSP126 are similar to the WW3 hindcast trend over the historical period 1981–2020 (Liu et al. 2022). That means there is projected to be a continuation of the trends seen over the last 40-years. For the high emissions SSP585 case, there is a stronger counter-clockwise rotation projected for most of the domain (Fig. 4i). This may be caused by the southward movement of Southern Ocean low-pressure systems (e.g., the southern annular mode) (Hemer et al. 2013c).

It is interesting to note that, although smaller H_s is projected in the nearshore regions of Victoria and New South Wales for SSP585 due to reduced local winds (Fig. S2), both T_p and D_p changes are projected to be larger. This is because both of these quantities are more influenced by changes in the Southern Ocean, where the wave climate is projected to increase more for SSP585 than SSP126 (Morim et al. 2018; Meucci et al. 2022).

4.2 Seasonality

The three wave parameters considered (H_s , T_p , D_p) and partitioned wave quantities were also each averaged seasonally over the historical and future time-slices. Their seasonal values and the corresponding projected changes are shown in Figs. 5, 6, 7, S3, S4. The historical period results show higher H_s (Fig. 5) with longer T_p (Fig. 6) in spring and winter than in summer and autumn, which is largely the result of the relative importance of swell (Fig. S3a, d) and wind-sea (Fig. S4a, d) in these respective seasons. Also, the D_p values (historical) off the coast of eastern Victoria turn from south-west

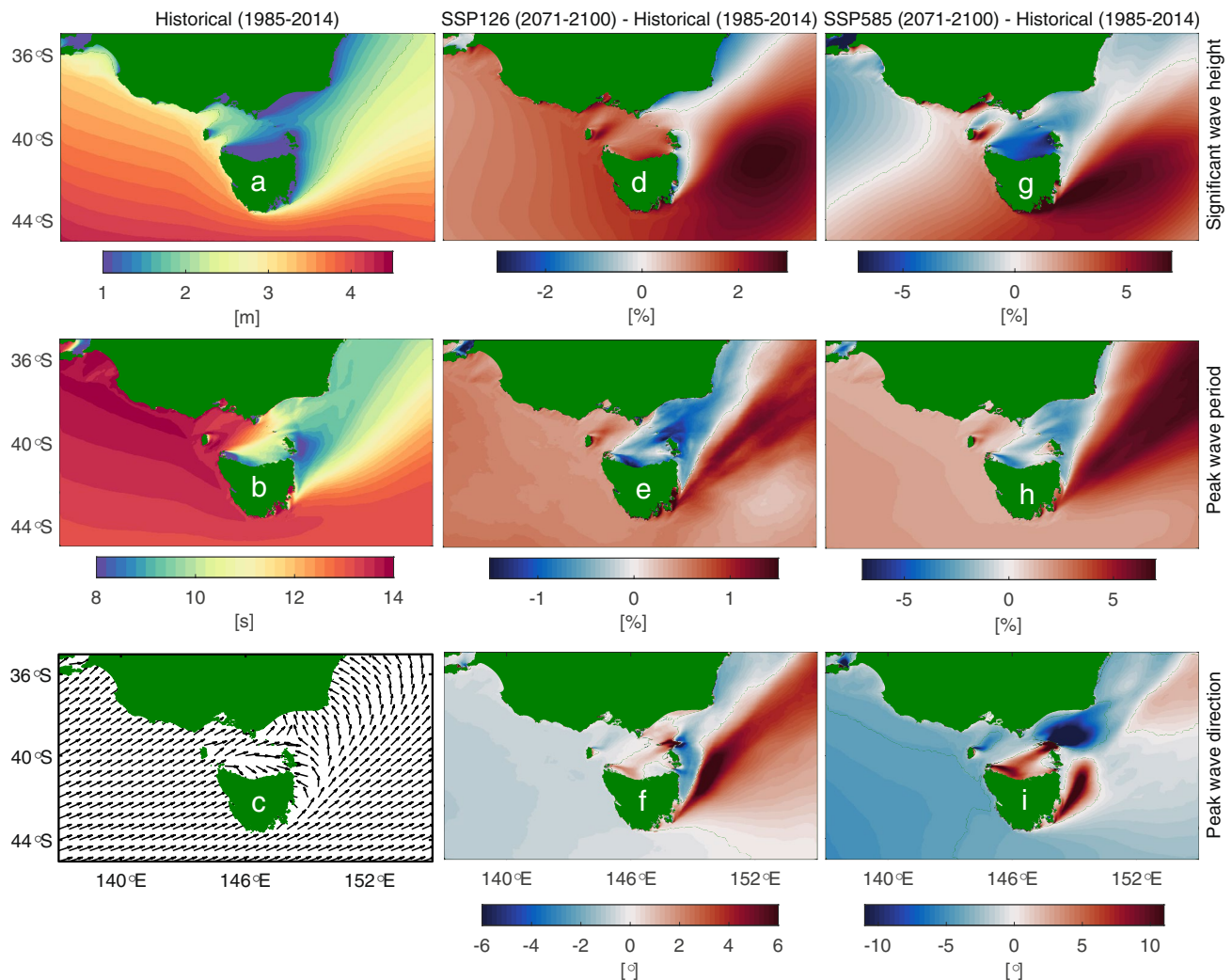


Fig. 4 Mean conditions of significant wave height, peak wave period and peak wave direction over the historical period 1985–2014 (**a–c**) and projected changes by the end of the twenty-first century 2071–2100 for (**d–f**) SSP126 and (**g–i**) SSP585. The projected changes (future – historical) of significant wave height and peak wave period

were normalized by the mean conditions in **a**, **b**, respectively. The projected changes (future – historical) of peak wave direction are direction differences between future and historical periods. Positive (negative) peak wave direction changes correspond to clockwise (counter-clockwise) rotation

in winter to south-east in summer (Fig. 7). These seasonal characteristics highlight the impacts of the Southern Ocean and the sheltering effects of Tasmania, which were reported by Liu et al. (2022).

The projected seasonal changes in H_s for SSP126 by the end of the twenty-first century (2071–2100) show a slight decrease in summer and an increase (up to 4%) in other seasons (Fig. 5e–h). The changes in SSP126 seasonal H_s values are a result of the projected changes in seasonality of the partitioned wave quantities, which shows relatively large changes in values of swell in autumn (Fig. S3g) and wind waves in spring and winter (Figs. S4e, h). The projected seasonal changes in H_s for SSP585, however, show the development of greater seasonality, with a decrease in summer and autumn (Fig. 5j, k) and an increase in spring

and winter (Fig. 5i, l). This is again consistent with the projected weakening of local winds. In spring and winter, the Southern Ocean swell systems dominate (Fig. S3i, l), whereas in summer and autumn the local winds dominate (Figs. S4j, k, S5j, k).

The projected seasonal changes in T_p for SSP126 show decreases in summer (Fig. 6f) and increases in the other seasons (Fig. 6e, g, h). Values of T_p for SSP585, however, show increasing values across all four seasons with larger changes than SSP126, which is a result of increasing Southern Ocean swell for SSP585 (Meucci et al. 2022). Bass Strait shows a decrease in T_p for both SSP126 and SSP585 in summer and winter as it is protected by Tasmania from the Southern Ocean.

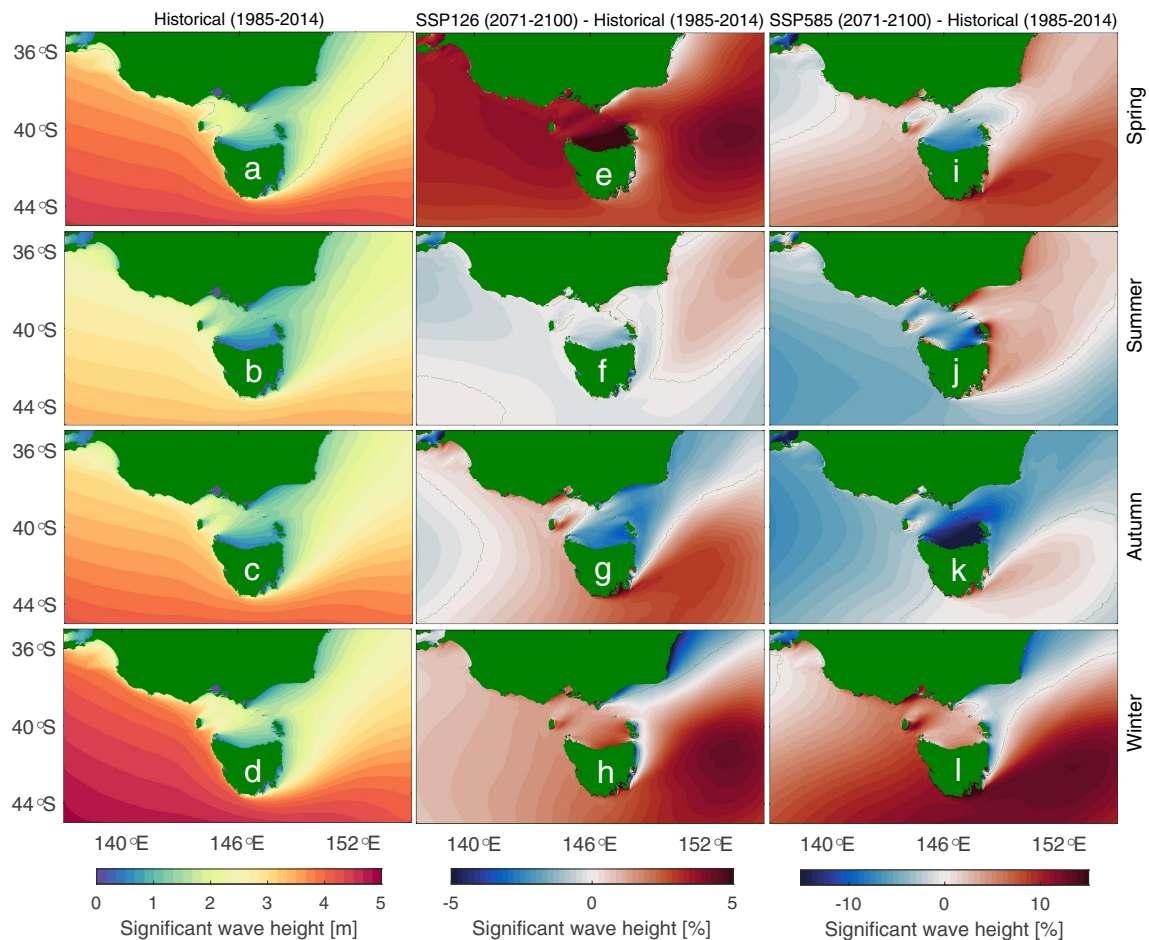


Fig. 5 Seasonal significant wave heights over the historical period 1985–2014 (a–d) and projected changes (future–historical, normalized by (a–d), respectively) by the end of the twenty-first century 2071–2100 for e–h SSP126 and i–l SSP585

The projections of seasonal D_p for the two scenarios show different patterns (Fig. 7e–l). The projected D_p for SSP126 reveals a slight counter-clockwise rotation ($\sim 2^\circ$) in autumn and almost no changes in the other seasons in the western regions of the domain. The projected D_p for SSP585, however, shows a clear counter-clockwise rotation ($\sim 3^\circ$ – 5°) in the west portion of the domain. This is most likely a result of the intensification of Southern Ocean swell for SSP585. Both scenarios show clear counter-clockwise rotation in summer and clockwise rotation in autumn and winter in the regions off north-eastern Tasmania with larger changes in SSP585 than SSP126. Such strong projected changes further emphasize the sheltering effects of Tasmania. In spring, however, the projected changes in D_p are clockwise to the east of Bass Strait for the two emission scenarios. This is possibly associated with the dynamic balance between swell and local wind (wind speed and wind direction) variations.

Nearshore industries and coastal ecosystem can be highly impacted by regional wave climate. Table S1 in the

Supplementary material, derived from Figs. 4, 5, 6, 7, tabulates the detailed historical values and projected changes of wave parameters at five long-term buoy locations. The SSP585 future projected wave climate results at these locations show a stronger seasonality than the SSP126 scenario. Changes in peak wave direction may critically affect the coastal equilibrium, changing beach erosion/accretion patterns. Further research is needed to investigate the relationship between the changes in wave direction and the state of the coastlines. Such research would greatly benefit coastal communities and inform effective climate change adaptation strategies.

4.3 Extreme wave analysis

An analysis of projected changes in extreme wave conditions was also conducted in the present study. Figure 8 shows the 90th-percentile (the top 10%) and 99th-percentile (the top 1%) H_s over the historical period (1985–2014) and their corresponding projected future changes. The magnitudes

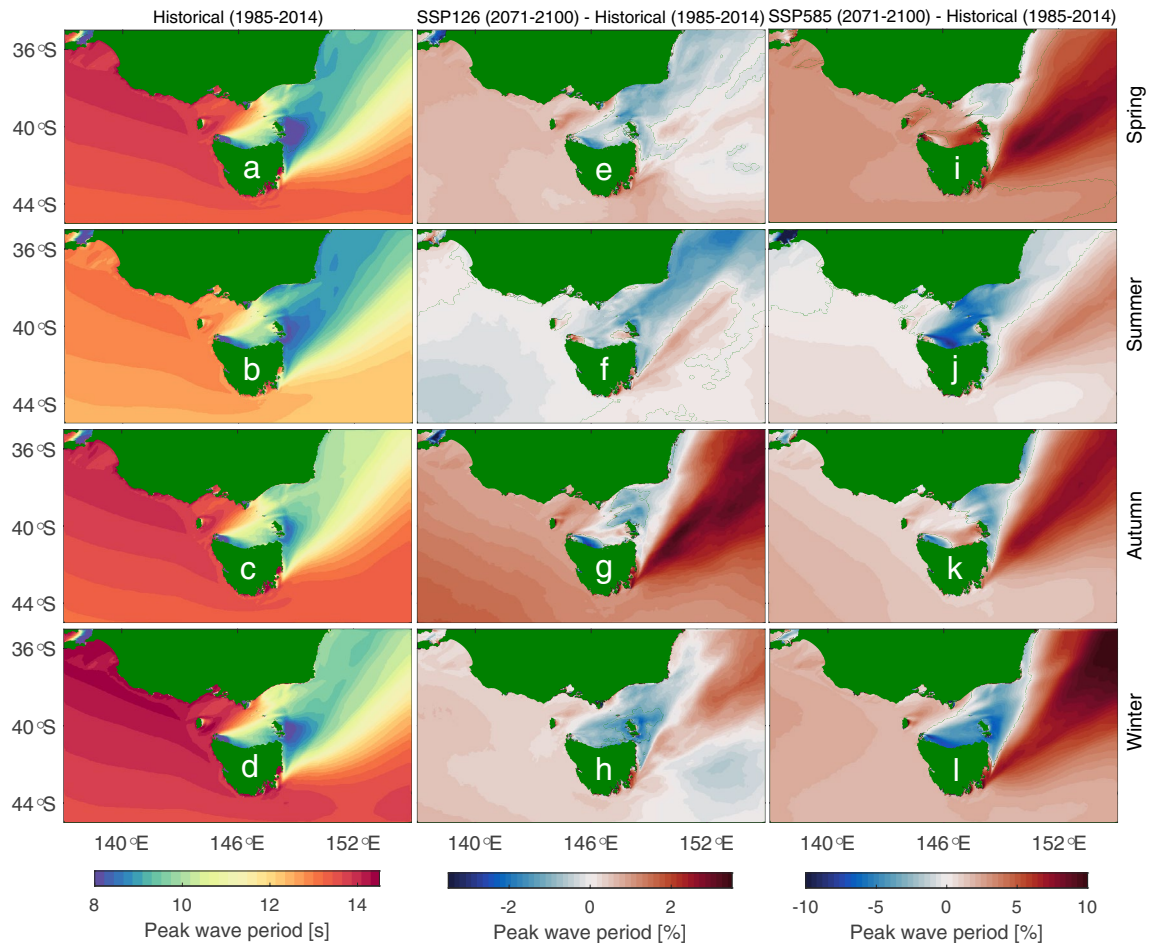


Fig. 6 Seasonal peak wave periods over the historical period 1985–2014 (a–d) and projected changes (future–historical, normalized by (a–d), respectively) by the end of the twenty-first century 2071–2100 for e–h SSP126 and i–l SSP585

of 90th-percentile and 99th-percentile H_s (historical) can reach ~6 m and ~8 m in the south-west part of the domain, respectively. This is consistent with the percentile values in Liu et al. (2022) for the ERA5-forced hindcast. Not surprisingly, the percentile changes of H_s for SSP585 are larger than for SSP126. This reflects the role the Southern Ocean has on the extreme wave conditions of the region. Interestingly, the magnitude of the percentage changes in the 99th percentile H_s for SSP126 is smaller than for the 90th percentile percentage changes. This indicates that the differences between the tails of the PDFs are decreasing at higher percentiles (i.e., smaller probabilities of exceedance).

In addition to the analysis of the upper percentile values, a POT-estimated extreme value analysis of H_s was also conducted to estimate projected changes as shown in Fig. 9. This figure shows the historical extreme H_s for return periods 10, 20, 50 and 100-years (Fig. 9a–d) as well as projected percentage changes for each of these cases for both SSP126 (Fig. 9e–h) and SSP585 (Fig. 9i–l). Over the historical period 1985–2014, the extreme value distributions

of H_s are similar to the percentile values in Fig. 8. The magnitudes of extreme H_s in the western and southern parts of the domain are very high due to the impact of the Southern Ocean swell, whilst Bass Strait and north-eastern parts of the domain show relatively smaller magnitude due to the protection provided by Tasmania. The largest magnitudes of the 100-year return period H_s reach up to 12.5 m in the southwest part of the domain. The estimated values in the south-western parts of the domain are ~4 to 8% higher than the corresponding values from the hindcast results of Liu et al. (2022), as a result of the higher values (overestimation) of the Southern Ocean swell in the climate model (Meucci et al. 2022).

The projected changes in the extreme value H_s for both SSP126 and SSP585 reveal a decrease in the western regions of the domain and an increase in the eastern domain (Fig. 9e–l). The projected percentage changes are larger for the higher return periods. For the region east of Bass Strait for SSP126, there is a projected percentage increase in

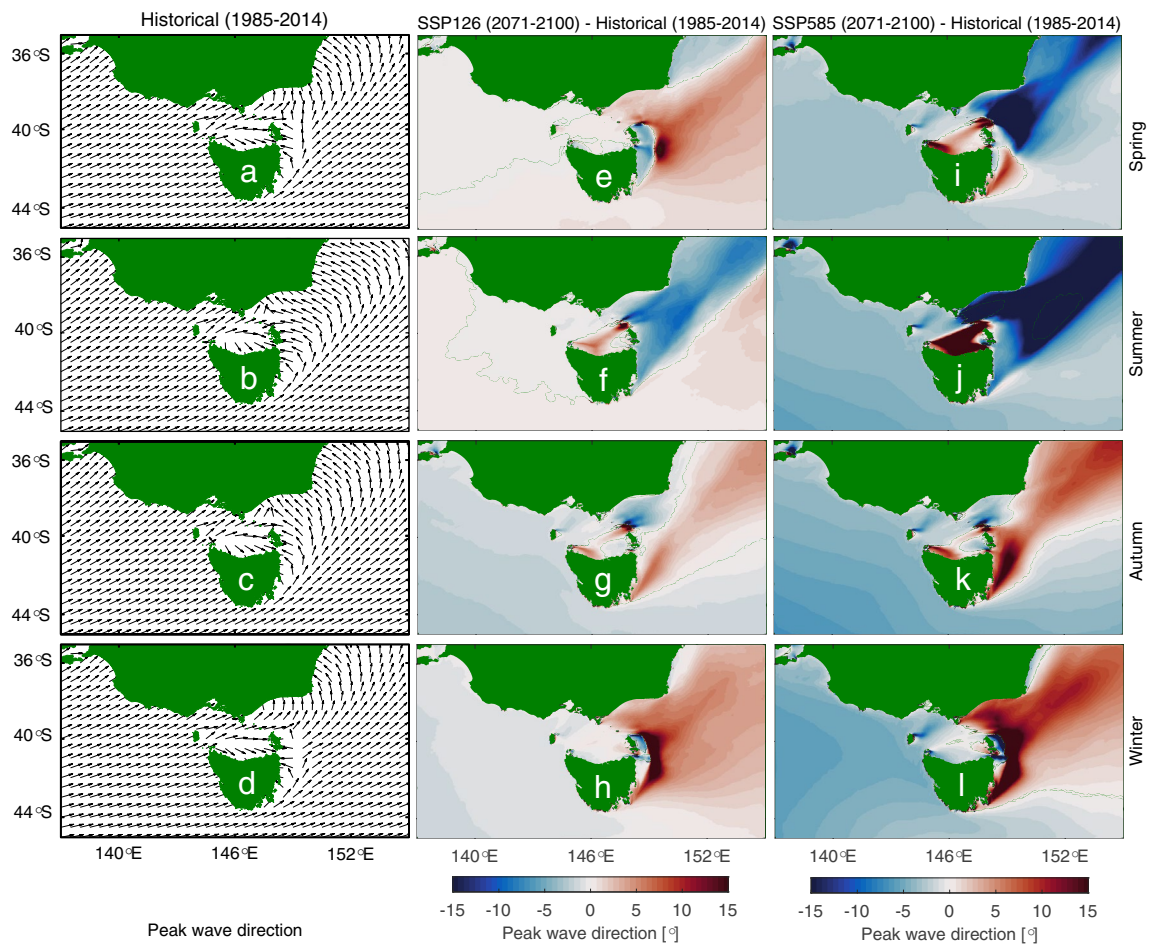


Fig. 7 Seasonal peak wave directions over the historical period 1985–2014 (**a–d**) and projected changes (future–historical) by the end of the twenty-first century 2071–2100 for **e–h** SSP126 and **i–l** SSP585. The projected changes (future–historical) of peak wave direction are

direction differences between future and historical periods. Note that negative (positive) changes in direction correspond to counter-clockwise (clockwise) rotation

extreme H_s . For SSP585, however, this same region shows a percentage decrease in extreme H_s .

Interestingly, the projected changes in extreme H_s in Fig. 9 are quite different to the upper percentile changes in Fig. 8. This is associated with the different calculation processes. When computing the extreme value H_s , only one peak from each storm is considered to ensure the data are independent. In contrast, a percentile considers all modeled data. Thus, the return period values do not consider storm duration.

The other consideration is, however, that even the 10-year return period values shown in Fig. 9 have a much lower probability of occurrence than the 99th percentile. As shown in Fig. 8, at lower percentiles, the future projections show an elevated tail of the PDF. However, this difference decreases as the probability of occurrence decreases (i.e., higher percentile). The results in Fig. 9 tend to indicate that at even lower probabilities of occurrence, the tails of the PDF cross

and projected future values are projected to decrease (in the western regions of the domain).

5 Conclusions

In this study, a high-resolution third-generation wave model (WW3 model) using unstructured grids was developed to investigate the projected future wave climate of Bass Strait and the south-east Australian region. The regional wave climate under two different greenhouse gas emission scenarios (mitigation scenario SSP126 and high-emission scenario SSP585) by the end of the twenty-first century (2071–2100) was projected and compared with the historical period (1985–2014). This regional WW3 climate model was nested within the GCM-forced global wave model of Meucci et al. (2022), and forced with ACCESS-CM2 surface wind speed.

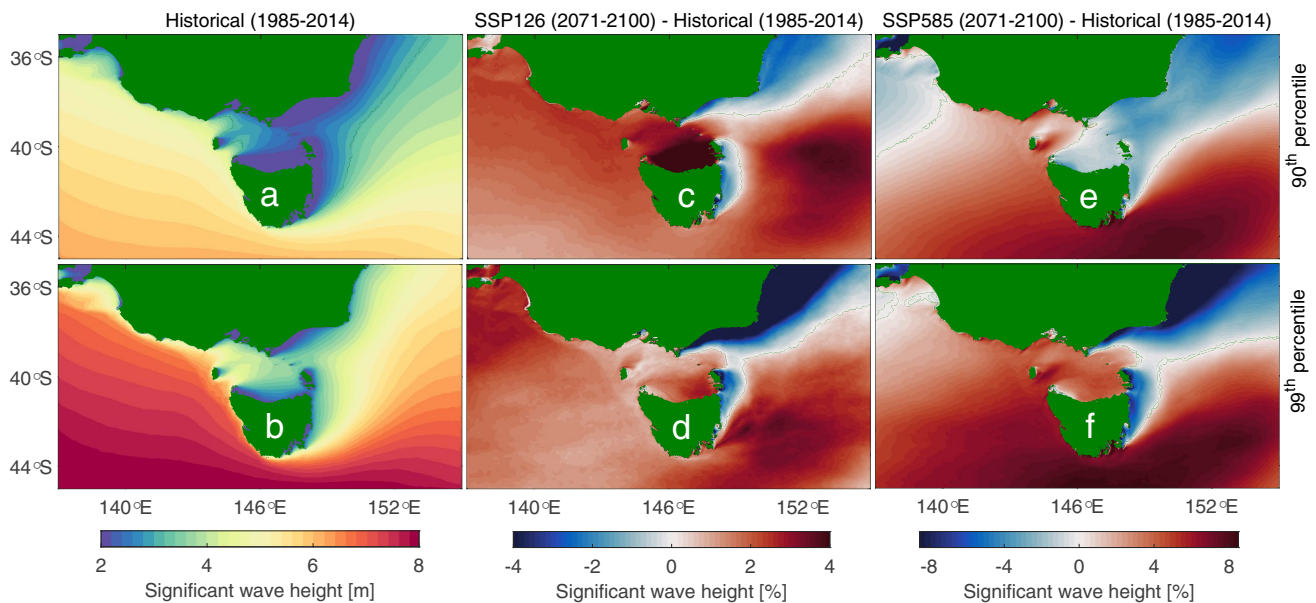


Fig. 8 90th percentile and 99th percentile significant wave height over the historical period 1985–2014 (**a**, **b**) and projected changes (future–historical, normalized by **a** and **b**, respectively) by the end of the twenty-first century 2071–2100 for **c**, **d** SSP126 and **e**, **f** SSP585

The present regional WW3 climate model was validated against the WW3 hindcast model dataset (Liu et al. 2022) and coastal long-term buoy observations. The comparison results show reasonable agreement with both datasets, though the historical H_s values are slightly higher (lower) in the south-western domain (Bass Strait and nearshore regions of eastern Victoria) due to overestimation of the Southern Ocean (underestimation of local winds). Also, the T_p and D_p differences between the WW3 climate model and buoy observations show that the climate model captures the historical climatology of the region, noting the limitations of GCM winds.

The projected mean values of H_s by the end of the twenty-first century for SSP126 show a slight increase (1–3%) across most of the domain, whilst the mean H_s for SSP585 shows a larger increase (up to 7%) in the offshore regions and a decrease (2%–3%) in the nearshore areas. The projected nearshore decreases are attributed to a projected decrease in the local wind (Fig. S2). Both scenarios (SSP126 and SSP585) show an increase across the domain in T_p as a result of projected increases in Southern Ocean swell. This projected increase in Southern Ocean swell also results in a counter-clockwise rotation (5°–10°) of D_p for SSP585. Such changes in D_p may have important effects on nearshore sediment transport and coastal morphology. The relationship between wave climate and beach erosion/accretion at both regional and global scales is an important area for future research.

Future projections of the seasonality show the different mechanisms controlling wave climate for the two scenarios.

The seasonal H_s for SSP585 is mainly impacted by wind sea in summer and autumn (Figs. S4), whilst the Southern Ocean swell dominates in spring and winter (Fig. S3). The projected seasonal T_p changes (Fig. 6) for both scenarios reveal the impacts of Southern Ocean swell, which is projected to increase in the future (both scenarios). Seasonal changes in D_p for SSP585 are projected to rotate counter-clockwise in the west part of the domain (Fig. 7).

The projected wave climate in the north-eastern part of the domain is complex. The wind speed is projected to decrease under the SSP585 scenario, causing a decrease in the wind-sea (Fig. S1). However, such changes in the local wind speed are not as evident in the SSP126 scenario. On the contrary, both SSP126 and SSP585 scenarios are consistent in projecting increasing intensity of the westerlies in the Southern Ocean. This translates into a consistent increase in swell approaching the model domain (Fig. S1). The swell increase is particularly evident in winter and spring (Figs. 5, 6) as the westerly wind belt moves closer to the domain of interest, and thus have a major impact on the wave climate.

The projected wave direction in the north-eastern part of the domain (Fig. 7) shows a clockwise shift in peak wave direction (D_p) in autumn and winter and a counterclockwise shift in summer and spring. Such changes may suggest both a latitudinal and longitudinal shift of the westerlies, impacting the wave direction in the region. This part of the model domain represents an area where future research would be valuable.

Extreme waves were also investigated and projected changes in upper percentile values show increases across

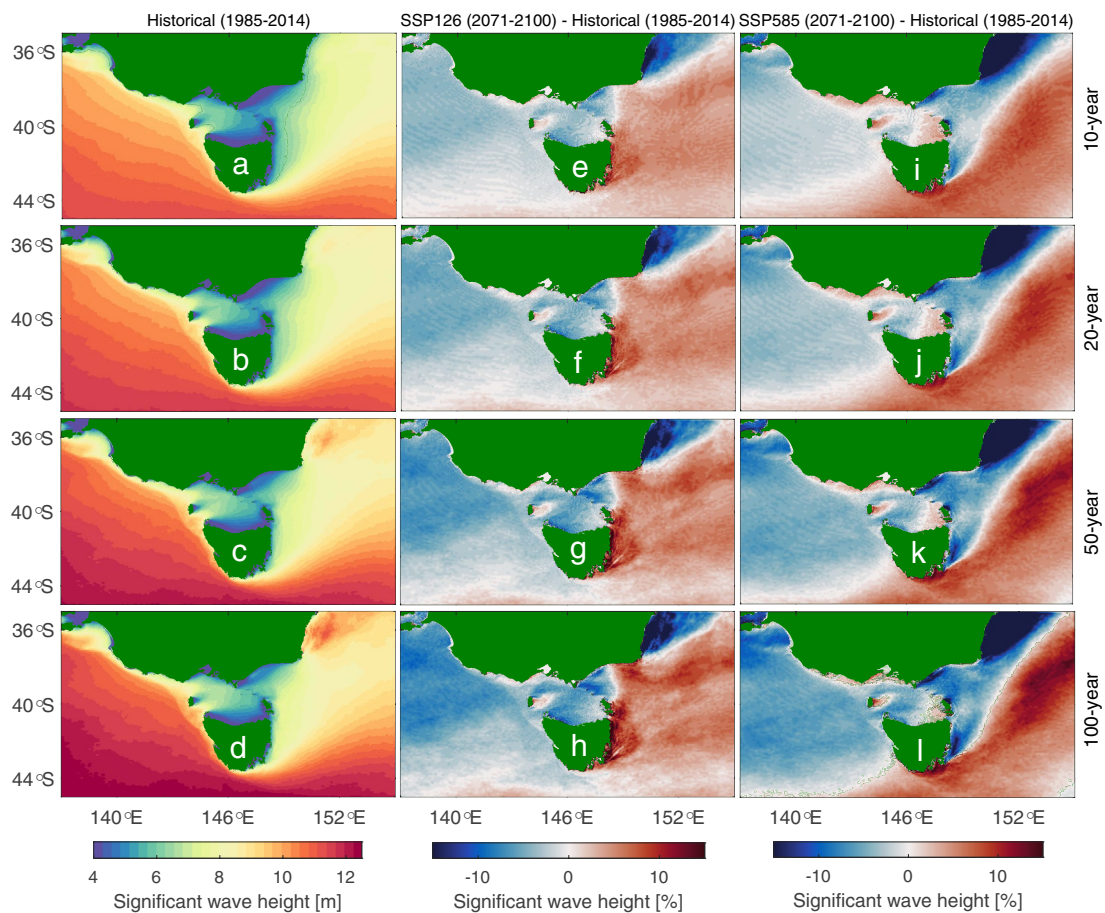


Fig. 9 Significant wave height based on different return periods over the historical period 1985–2014 (**a–d**) and projected changes (future–historical, normalized by (**a–d**), respectively) by the end of

the twenty-first century 2071–2100 for **e–h** SSP126 and **i–l** SSP585. The return periods are shown on the right

the domain for both scenarios. Nearshore regions from Batemans Bay to Lakes Entrance are impacted by local winds and thus show a projected decrease in the future. The POT-based extreme value analysis of H_s for SSP126 projects a decrease in extreme H_s in the western regions of the domain and an increase in the east (Fig. 9). Extreme H_s values for SSP585 are, however, projected to decrease from Batemans Bay to east of Tasmania (Fig. 9).

Supplementary Information The online version contains supplementary material available at <https://doi.org/10.1007/s00382-022-06310-4>.

Acknowledgements We acknowledge the WW3 development group for providing source codes and the University of Melbourne for providing the high-performance computer cluster. We also thank Huy Quang Tran for sharing the combined bathymetric data. Wave buoy data were provided by the Port of Melbourne and Gippsland Ports. Australian Ocean Data Network (AODN) wave data were sourced from Australia's Integrated Marine Observing System (IMOS)—IMOS is enabled by the National Collaborative Research Infrastructure Strategy (NCRIS). Wind data were provided by Climate Data Store.

Author Contributions JL: Conceptualization, Data Curation, Formal Analysis, Investigation, Methodology, Resources, Software, Validation, Visualization, Writing—Original Draft, Writing—Review & Editing. AM: Data Curation, Investigation, Methodology, Writing—Review & Editing. IRY: Conceptualization, Data Curation, Funding Acquisition, Methodology, Project Administration, Resources, Software, Supervision, Writing—Original Draft, Writing—Review & Editing.

Funding Open Access funding enabled and organized by CAUL and its Member Institutions. Ian R. Young thanks the Victorian Coastal Monitoring Program with provided funding through the Department of Environment, Land, Water and Planning and the University of Melbourne and Deakin University. Jin Liu acknowledges the support of the Melbourne Research Scholarship provided by the University of Melbourne.

Data availability The observation and model input data used in this study are open access and were properly cited. The model-derived data are available upon request from the corresponding author.

Code availability MATLAB was adopted to analysis the data in the present study.

Declarations

Conflict of interest The authors have no relevant financial or non-financial interests to disclose.

Open Access This article is licensed under a Creative Commons Attribution 4.0 International License, which permits use, sharing, adaptation, distribution and reproduction in any medium or format, as long as you give appropriate credit to the original author(s) and the source, provide a link to the Creative Commons licence, and indicate if changes were made. The images or other third party material in this article are included in the article's Creative Commons licence, unless indicated otherwise in a credit line to the material. If material is not included in the article's Creative Commons licence and your intended use is not permitted by statutory regulation or exceeds the permitted use, you will need to obtain permission directly from the copyright holder. To view a copy of this licence, visit <http://creativecommons.org/licenses/by/4.0/>.

References

- Akpınar A, Bingölbalı B, Van Vledder GP (2016) Wind and wave characteristics in the Black Sea based on the SWAN wave model forced with the CFSR winds. *Ocean Eng* 126:276–298. <https://doi.org/10.1016/j.oceaneng.2016.09.026>
- Battjes JA, Janssen J (1978) Energy loss and set-up due to breaking of random waves. *Coast Eng* 1978:569–587. <https://doi.org/10.1061/9780872621909.034>
- Beguiria S (2005) Uncertainties in partial duration series modelling of extremes related to the choice of the threshold value. *J Hydrol* 303:215–230. <https://doi.org/10.1016/j.jhydrol.2004.07.015>
- Bi D, Dix M, Marsland S, O'Farrell S, Sullivan A, Bodman R, Law R, Harman I, Srbinovsky J, Rashid HA, Dobrohotoff P, Mackallah C, Yan H, Hirst A, Savita A, Boeira Dias F, Woodhouse M, Fiedler R, Heerdegen A (2020) Configuration and spin-up of ACCESS-CM2, the new generation Australian Community Climate and Earth System Simulator Coupled Model. *J South Hemisph Earth Syst Sci* 70:225–251. <https://doi.org/10.1071/es19040>
- Caires S, Sterl A (2005) 100-year return value estimates for ocean wind speed and significant wave height from the ERA-40 data. *J Clim* 18:1032–1048. <https://doi.org/10.1175/jcli-3312.1>
- Casas-Prat M, Sierra J (2013) Projected future wave climate in the NW Mediterranean Sea. *J Geophys Res Oceans* 118:3548–3568. <https://doi.org/10.1002/jgrc.20233>
- Cavaleri L, Rizzoli PM (1981) Wind wave prediction in shallow water: theory and applications. *J Geophys Res Oceans* 86:10961–10973. <https://doi.org/10.1029/jc086ic11p10961>
- Coles S, Bawa J, Trenner L, Dorazio P (2001) An introduction to statistical modeling of extreme values. Springer, Berlin. <https://doi.org/10.1007/978-1-4471-3675-0>
- De Leo F, Besio G, Mentaschi L (2021) Trends and variability of ocean waves under RCP8.5 emission scenario in the Mediterranean Sea. *Ocean Dyn* 71:97–117. <https://doi.org/10.1007/s10236-020-01419-8>
- Hasselmann K, Barnett TP, Bouws E, Carlson H, Cartwright DE, Enke K, Ewing JA, Gienapp H, Hasselmann DE, Kruseman P, Meerburg A, Müller P, Olbers DJ, Richter K, Sell W, Walden H (1973) Measurements of wind-wave growth and swell decay during the Joint North Sea Wave Project (JONSWAP). *Ergänzungsheft*
- Hemer MA, Trenham CE (2016) Evaluation of a CMIP5 derived dynamical global wind wave climate model ensemble. *Ocean Model* 103:190–203. <https://doi.org/10.1016/j.ocemod.2015.10.009>
- Hemer MA, McInnes KL, Ranasinghe R (2012) Climate and variability bias adjustment of climate model-derived winds for a southeast Australian dynamical wave model. *Ocean Dyn* 62:87–104. <https://doi.org/10.1007/s10236-011-0486-4>
- Hemer M, McInnes K, Ranasinghe R (2013a) Projections of climate change-driven variations in the offshore wave climate off south eastern Australia. *Int J Climatol* 33:1615–1632. <https://doi.org/10.1002/joc.3537>
- Hemer MA, Fan Y, Mori N, Semedo A, Wang XL (2013b) Projected changes in wave climate from a multi-model ensemble. *Nat Clim Chang* 3:471–476. <https://doi.org/10.1038/NCLIMATE1791>
- Hemer MA, Katzfey J, Trenham CE (2013c) Global dynamical projections of surface ocean wave climate for a future high greenhouse gas emission scenario. *Ocean Model* 70:221–245. <https://doi.org/10.1016/j.ocemod.2012.09.008>
- Hersbach H, Bell B, Berrisford P, Hirahara S, Horányi A, Muñoz-Sabater J, Nicolas J, Peubey C, Radu R, Schepers D (2020) The ERA5 global reanalysis. *Q J R Meteorol Soc* 146:1999–2049. <https://doi.org/10.1002/qj.3803>
- Kirezci E, Young IR, Ranasinghe R, Muis S, Nicholls RJ, Lincke D, Hinkel J (2020) Projections of global-scale extreme sea levels and resulting episodic coastal flooding over the 21st Century. *Sci Rep* 10:1–12. <https://doi.org/10.1038/s41598-020-67736-6>
- Liu Q, Rogers WE, Babanin AV, Young IR, Romero L, Zieger S, Qiao F, Guan C (2019) Observation-based source terms in the third-generation wave model WAVEWATCH III: updates and verification. *J Phys Oceanogr* 49:489–517. <https://doi.org/10.1175/JPO-D-18-0137.1>
- Liu Q, Babanin A, Rogers W, Zieger S, Young I, Bidlot J, Durrant T, Ewans K, Guan C, Kirezci C, Lemos G, MacHutchon K, Moon I, Rapizo H, Ribal A, Semedo A, Wang J (2021) Global wave hindcasts using the observation-based source terms: description and validation. *J Adv Model Earth Syst*. <https://doi.org/10.1029/2021MS002493>
- Liu J, Meucci A, Liu Q, Babanin AV, Ierodiaconou D, Young IR (2022) The wave climate of Bass Strait and south-east Australia. *Ocean Model*. <https://doi.org/10.1016/j.ocemod.2022.101980>
- Lobeto H, Menendez M, Losada JJ (2021) Future behavior of wind wave extremes due to climate change. *Sci Rep* 11:1–12. <https://doi.org/10.1038/s41598-021-86524-4>
- Meucci A, Young IR, Hemer M, Kirezci E, Ranasinghe R (2020) Projected 21st century changes in extreme wind-wave events. *Sci Adv* 6:eaa7295. <https://doi.org/10.1126/sciadv.aaz7295>
- Meucci A, Young IR, Hemer M, Trenham C, Watterson IG (2022) 140 years of global ocean wind-wave climate derived from CMIP6 ACCESS-CM2 and EC-Earth3 GCMs: Global trends, regional changes, and future projections. *J Clim* (Under review)
- Morim J, Cartwright N, Etemad-Shahidi A, Strauss D, Hemer M (2016) Wave energy resource assessment along the Southeast coast of Australia on the basis of a 31-year hindcast. *Appl Energy* 184:276–297. <https://doi.org/10.1016/j.apenergy.2016.09.064>
- Morim J, Hemer M, Cartwright N, Strauss D, Andutta F (2018) On the concordance of 21st century wind-wave climate projections. *Glob Planet Change* 167:160–171. <https://doi.org/10.1016/j.gloplacha.2018.05.005>
- Morim J, Hemer M, Wang XL, Cartwright N, Trenham C, Semedo A, Young I, Bricheno L, Camus P, Casas-Prat M, Erikson L, Mentaschi L, Mori N, Shimura T, Timmermans B, Aarnes O, Breivik Ø, Behrens A, Dobrynin M, Menendez M, Staneva J, Wehner M, Wolf J, Kamranzad B, Webb A, Stopa J, Andutta F (2019) Robustness and uncertainties in global multivariate wind-wave climate projections. *Nat Clim Chang* 9:711–718. <https://doi.org/10.1038/s41558-019-0542-5>
- O'Grady J, Hemer M, McInnes K, Trenham C, Stephenson A (2021) Projected incremental changes to extreme wind-driven wave

- heights for the twenty-first century. *Sci Rep* 11:1–8. <https://doi.org/10.1038/s41598-021-87358-w>
- Roberts KJ, Pringle WJ, Westerink J (2019) OceanMesh2D 1.0: MATLAB-based software for two-dimensional unstructured mesh generation in coastal ocean modeling. *Geosci Model Dev* 12:1847–1868. <https://doi.org/10.5194/gmd-12-1847-2019>
- Rogers WE, Babanin AV, Wang DW (2012) Observation-consistent input and whitecapping dissipation in a model for wind-generated surface waves: description and simple calculations. *J Atmos Ocean Sci* 29:1329–1346. <https://doi.org/10.1175/jtech-d-11-00092.1>
- Shimura T, Mori N, Mase H (2015) Future projection of ocean wave climate: analysis of SST impacts on wave climate changes in the western North Pacific. *J Clim* 28:3171–3190. <https://doi.org/10.1175/JCLI-D-14-00187.1>
- Takbash A, Young IR (2019) Global ocean extreme wave heights from spatial ensemble data. *J Clim* 32:6823–6836. <https://doi.org/10.1175/JCLI-D-19-0255.1>
- Takbash A, Young IR, Breivik Ø (2019) Global wind speed and wave height extremes derived from long-duration satellite records. *J Clim* 32:109–126. <https://doi.org/10.1175/JCLI-D-18-0520.1>
- Watterson I (2015) Improved simulation of regional climate by global models with higher resolution: skill scores correlated with grid length. *J Clim* 28:5985–6000. <https://doi.org/10.1175/JCLI-D-14-00702.1>
- WW3DG (2019) User manual and system documentation of WAVEWATCH III version 6.07.
- Young IR (1994) On the measurement of directional wave spectra. *Appl Ocean Res* 16:283–294. [https://doi.org/10.1016/0141-1187\(94\)90017-5](https://doi.org/10.1016/0141-1187(94)90017-5)
- Young IR, Ribal A (2019) Multiplatform evaluation of global trends in wind speed and wave height. *Science* 364:548–552. <https://doi.org/10.1126/science.aav9527>
- Young IR, Fontaine E, Liu Q, Babanin AV (2020) The wave climate of the Southern Ocean. *J Phys Oceanogr* 50:1417–1433. <https://doi.org/10.1175/JPO-D-20-0031.1>
- Zieger S, Babanin AV, Rogers WE, Young IR (2015) Observation-based source terms in the third-generation wave model WAVEWATCH. *Ocean Model* 96:2–25. <https://doi.org/10.1016/j.ocemod.2015.07.014>

Publisher's Note Springer Nature remains neutral with regard to jurisdictional claims in published maps and institutional affiliations.